How to cite: *Angew. Chem. Int. Ed.* **2022,** *61,* e202206564
International Edition: doi.org/10.1002/anie.202206564
German Edition: doi.org/10.1002/ange.202206564

COFs Hot Paper

Ultrathin Covalent Organic Framework Anchored on Graphene for Enhanced Organic Pollutant Removal

*Changxia Li, Patrick Guggenberger, Seung Won Han, Wei-Lu Ding, and Freddy Kleitz**

Abstract: Covalent organic frameworks (COFs) are of great potential as adsorbents owing to their tailorable functionalities, low density and high porosity. However, their intrinsically stacked two-dimensional (2D) structure limits the full use of their complete surface for sorption, especially the internal pores. The construction of ultrathin COFs could increase the exposure of active sites to the targeted molecules in a pollutant environment. Herein, an ultrathin COF with a uniform thickness of ca. 2 nm is prepared employing graphene as the surface template. The resulting hybrid aerogel with an ultralow density (7.1 mg cm^{-3}) exhibits the ability to remove organic dye molecules of different sizes with high efficiency. The three-dimensional (3D) macroporous structure and well-exposed adsorption sites permit rapid diffusion of solution and efficient adsorption of organic pollutants, thereby, greatly contributing to its enhanced uptake capacity. This work highlights the effect of COF layer thickness on adsorption performance.

Introduction

Due to increasing industrialization, water pollution is causing great damage to the environment, where industrial wastewater containing organic pollutants is a primary source of the contamination.[1] These industrial pollutants, e.g. organic dyes, are usually highly water-soluble, non-degradable, and many are toxic and carcinogenic.[2,3] Their discharge into the environment has generated an enormous threat to populations, ecosystems, and living organisms. To address this issue, diverse materials such as carbons,[4,5] zeolites,[6] metal–organic frameworks (MOFs),[7,8] and porous organic polymers,[9] have been used as adsorbents to remove organic pollutants from aqueous media. Amongst various porous adsorbents, covalent organic frameworks (COFs) have recently been the focus of a number of studies because of their promising characteristics, including low density, high chemical stability, permanent porosity, and designable pore functionality.[10–15] In the design of COF-based adsorbents, one key issue that needs to be taken more thoroughly into account is the required pore size and pore accessibility for a given dye molecule, i.e., whether the dye molecule can easily gain access to the inside of the pores. The majority of the COFs currently reported are furnished with one-dimensional (1D) channels with an aperture size in the range of 1–4 nm.[16–20] The micropore or small mesopore characteristics and the highly stacked nature of the structure restrict the dye molecules from quickly entering the interior of the pores, with some materials even suffering from pore blockage during dye adsorption, which leads to low water purification efficiency.

Synthesizing ultrathin COF nanosheets can maximize the accessibility of active sites and accelerate mass transport.[21,22] For example, the lithium storage capacity of exfoliated redox-active COF nanosheets with a thickness of 3–5 nm was doubled or tripled compared to the native COF bulk powder at the same current rate because the exfoliated COFs enabled rapid Li^+ transport and shorter diffusion pathways.[23] Therefore, ultrathin COF nanosheets have the potential to enhance both the exposure of adsorption active sites and thus the purification efficiency for organic pollutants. However, to the best of our knowledge, no report has focused on the design of 2D ultrathin COF sorbents for organic pollutants removal.

Thus far, efforts have been made to synthesize ultrathin COF nanosheets through various methods, including the top-down exfoliation strategy from bulk counterparts, which takes advantage of ball milling,[23] solvent-assisted sonication,[24] or chemical exfoliation,[25] and bottom-up synthesis strategies, such as interfacial synthesis[26–28] and on-surface synthesis.[29] However, neither strategy is suitable for large-scale preparation of the target products because the former usually leads to uncontrollable thickness with very low yields, while the latter requires very dilute concentration

[*] Dr. C. Li, P. Guggenberger, Prof. Dr. F. Kleitz
Department of Inorganic Chemistry—Functional Materials, Faculty of Chemistry, University of Vienna
Währinger Straße 42, 1090 Vienna (Austria)
E-mail: freddy.kleitz@univie.ac.at
Dr. S. W. Han
Center for Nanomaterials and Chemical Reactions, Institute for Basic Science (IBS)
Daejeon, 34141 (South Korea)
Dr. W.-L. Ding
Beijing Key Laboratory of Ionic Liquids Clean Process, CAS Key Laboratory of Green Process and Engineering, Institute of Process Engineering, Chinese Academy of Sciences
Beijing 100190 (China)

of precursors and long reaction time (e.g., a few days, even one month). As a result, the preparation of uniform ultrathin COF nanosheets with controllable thickness on a large scale is highly desired, but it is still a huge challenge.

In our recent efforts, an ultralight anthraquinone-based COF/graphene aerogel was produced successfully through a facile hydrothermal method.[30] The resulting aerogel with hierarchical porous structure exhibited outstanding capacitive performance and adsorption capacity for organic solvents. Herein, based on this hydrothermal method, an ultrathin COF containing sulfonate ions with a uniform thickness of 2 nm is obtained using graphene oxide (GO) as the template. The composite aerogel exhibits a hierarchical porous structure, in which the interlinked graphene framework provides macroporous channels, while the anionic COF affords microporosity and charged surfaces. Moreover, for the first time, the relationship between COF layer thickness and dye removal performance is explored. In comparison to bulk COF powder, the anionic ultrathin COF/graphene aerogel (CGA) shows much faster removal of cationic organic pollutants. Taking Rhodamine B dye as an example, >99 % of the dye could be captured within 3 minutes using the CGA adsorbent, while it takes as much as 3 hours for the bulk COF powder.

Results and Discussion

In order to illustrate the advantages of ultrathin COF with 3D pore channels, the bulk sulfonate anionic COF (COF-SO_3Na) was first synthesized for comparison. The pure COF powder was prepared using a hydrothermal method, in which 1,3,5-triformylphloroglucinol (Tp) and sodium 2,5-diaminobenzenesulfonate (DB-SO_3Na) serve as the reaction monomers, water as the solvent, and *p*-toluenesulfonic acid (PTSA) as the catalyst (Figures 1a and S1a). This mixture was shaken for 20 minutes using a vortex shaker, and then the orange solution was transferred to an autoclave and heated at 120 °C for 24 hours. After washing and drying, a dark-red powder is produced. The crystalline structure of COF-SO_3Na was confirmed by powder X-ray diffraction (XRD). The visible diffraction peaks at $2\theta = 4.7°$ (100), 8.1° (210), and 26.8° (001) match well with the simulated AA stacking model,[31,32] suggesting the successful formation of COF-SO_3Na using the hydrothermal method (Figure 1b). Moreover, after immersing the fresh sample in various solvents (e.g., dimethylacetamide, ethanol, acetone, H_2O, 1 M HNO_3, or 3 M NaOH) for 2 days, the XRD patterns are almost identical to that of the original, demonstrating the chemical stability of COF-SO_3Na (Figure S2). N_2 physisorption isotherm was measured to quantify the specific surface area and the pore size distribution of the COF-SO_3Na powder (Figures S3 and S4). The Brunauer–Emmett–Teller specific surface area (S_{BET}) is 179 $m^2 g^{-1}$, which is comparable to both the corresponding COF membrane (212 $m^2 g^{-1}$)[31] obtained through interfacial synthesis and the corresponding COF powder (159–215 $m^2 g^{-1}$)[32,33] prepared using the solvothermal method. The relatively low specific surface area might be attributed to steric hindrance caused by the bulkiness of the functional sulfonate ions. The pore size distribution, as determined by the quenched solid density functional theory (QSDFT) model, shows a maximum at 1.36 nm, which is close to its theoretical pore size (1.41 nm).[31] Scanning electron microscopy (SEM) and the corresponding energy-dispersive spectroscopy (EDS) mapping images reveal that this COF features a fiber-like morphology with a length of several micrometers and a diameter of around 100–200 nm, as well as a uniform distribution of C, O, N, S, and Na (Figures 1c and S5).

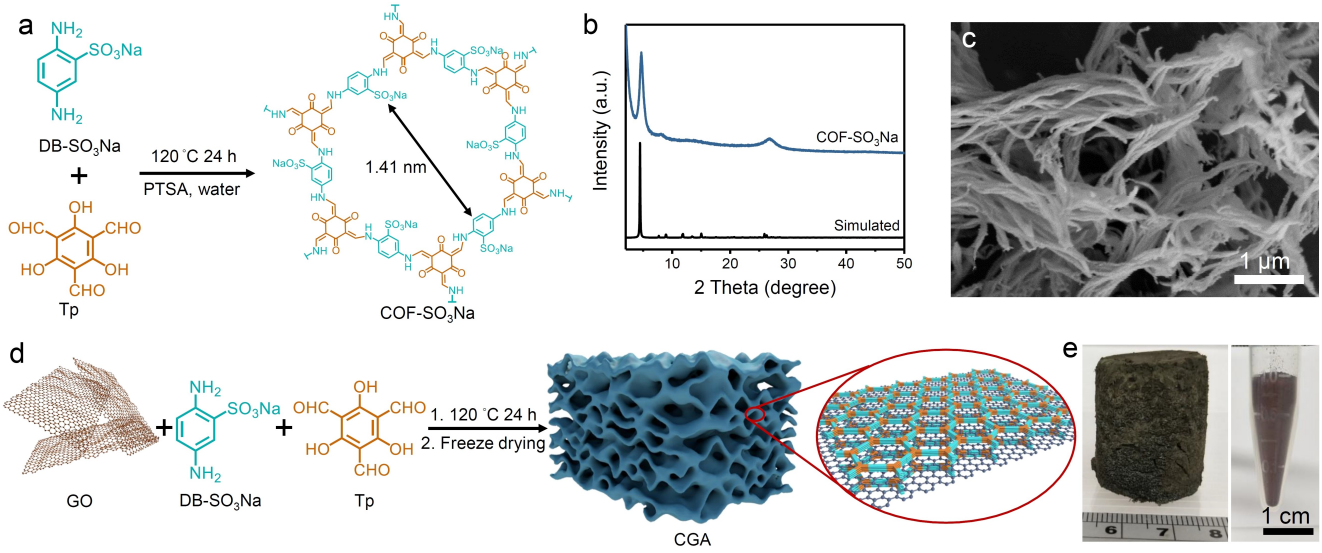

Figure 1. a) Formation and pore structure of COF-SO_3Na. b) Powder XRD pattern of bulk COF-SO_3Na. The simulated pattern is presented as reference. c) SEM image of bulk COF-SO_3Na. d) The synthesis procedure for CGA. e) Photographs of the CGA (left) and the bulk COF-SO_3Na powder (right).

To construct ultrathin COF-SO_3Na with 3D porous architecture, GO was introduced as a template during the hydrothermal synthesis to obtain COF/reduced graphene oxide (RGO) hybrid aerogel (Figures 1d and S1b). The procedure includes the in situ growth of a few layers of COF on the graphene template and the reduction of the GO (Figure S6) during the hydrothermal process as well as subsequent washing and freeze-drying treatment. Figure 1e shows CGA and COF powder with the same weight (ca. 102 mg), but the density of CGA (ca. 7.1 mg cm^{-3}) is only about one-fourteenth of that of the bulk COF powder (ca. 102 mg cm^{-3}).

The morphology of CGA was observed by SEM and transmission electron microscopy (TEM). As shown in Figure 2a, b, the CGA displays an interlinked macroporous structure with a channel size of several micrometers. TEM images exhibit a transparent appearance, demonstrating its low thickness (Figure 2c, d). No isolated COF fibers or particles were detected, offering a first clue that COF-SO_3Na grows only along the graphene surface. The SEM elemental mapping images confirm the even distribution of N, O, S, and Na over the whole area (Figure 2e). In addition, scanning TEM (STEM) mapping images further indicate the elemental distribution on a single hybrid nanosheet (Figure S7). Both mapping images offer a second clue of the uniform loading of COF-SO_3Na on the graphene surface. Furthermore, this conclusion is directly supported by atomic force microscopy (AFM) analysis, which shows that the CGA nanosheets possess an average thickness of ca. 4.6 nm, while the thickness of pure RGO sheets is ca. 2.6 nm (Figure 2f, g and Figure S8). The thickness increase of 2.0 nm means that approx. four layers of COF-SO_3Na are immobilized on the graphene surface based on its theoretical interlayer spacing (5.157 Å) calculated from the simulated structure.[31,32] XRD and Fourier transform infrared (FT-IR) measurements also reveal the effective growth of COF on the graphene template (Figure 2h, i). In the XRD results, CGA shows a much weaker peak at 4.7° (2θ) compared to pure COF due to the rather thin layer of COF on the graphene surface. Notably, the broad wide-angle diffraction peak of CGA at 26.0° (2θ), assigned to π–π stacking between different layers, is located between that of RGO (24.0°) and COF (26.8°) and closer to pure COF, indicating again that the graphene sheets are covered by the COF. FT-IR spectra display the similar characteristic peaks at 1569 and 1210 cm^{-1} for COF and CGA, which belong to the C=C and C–N stretching vibration bands (Figure 2i). In addition, the characteristic peaks at 1433, 1077, 1024 and 986 cm^{-1} are attributed to the stretching band of O=S=O, proving the presence of sulfonate groups. Overall, the above experimental results demonstrate the successful formation of a 3D COF/RGO aerogel with ultrathin COF layers anchored on graphene nanosheets.

The contents and thickness of COF-SO_3Na can readily be adjusted by tuning the amount of COF precursors used during the preparation. The composite aerogels are marked as CGA-x, x representing the average thickness of the hybrid nanosheets (i.e., 3.3 nm, 3.8 nm, 4.6 nm, and 5.5 nm) as confirmed from the AFM measurements (Figures S9–S11). If not otherwise mentioned, the CGA discussed here

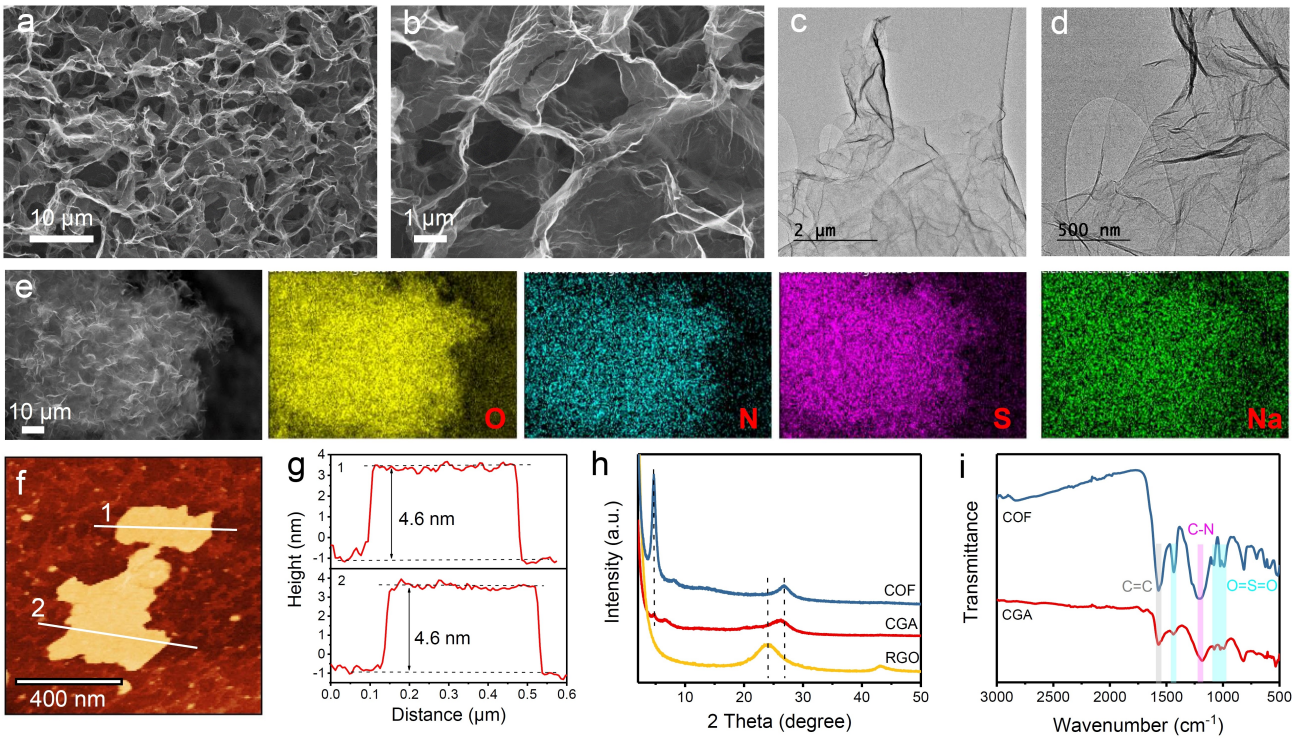

Figure 2. a), b) SEM images and c), d) TEM images of CGA. e) SEM image and the corresponding elemental mapping of CGA. f), g) AFM image and the corresponding height profiles of CGA. h) XRD patterns of COF-SO_3Na, CGA and RGO. i) FT-IR spectra of COF-SO_3Na and CGA.

refers to the 4.6 nm thickness. The loading amount of COF within hybrid aerogels can be calculated based on elemental analysis (Table S2). As the amount of COF-SO_3Na increases, the 3D aerogels become more expanded (Figure S12a). However, when the thickness of the hybrid nanosheets increased to 5.5 nm, the aerogel lost its well-defined shape. With the increase in COF coverage, the peak at 3.4° (2θ) in the XRD patterns becomes more and more obvious (Figure S12b). FT-IR spectra show identical characteristic peaks for all the hybrid aerogels (Figure S12c). From the SEM images, all these aerogels present a 3D macroporous architecture (Figure S13). Furthermore, N_2 adsorption measurements were performed to determine S_{BET} and the porosity characteristics of the composite aerogels (Figures S14 and S15). All hybrid materials show moderate S_{BET} of 149–185 $m^2 g^{-1}$ and that value rises gradually with increasing COF loading (the parameters are summarized in Table S3). Nevertheless, CGA-5.5 shows a slightly decreased S_{BET} which might be attributed to the fact that the well-defined shape of the hydrogel is not fully preserved at high COF loading because of the weakened interaction between the nanosheets[30] (Figure S12a). Therefore, CGA-4.6 presents the largest S_{BET} of 185 $m^2 g^{-1}$. In addition, all as-synthesized composite aerogels possess low densities ranging from approximately 7.1 to 10.6 mg cm^{-3} (Table S3). Thermogravimetric analysis (TGA) displays the thermal stability of composite aerogels under a N_2 atmosphere, and weight retention ranges within 49–72 % after heating up to 800 °C (Figure S16). These results further confirm the formation of ultrathin COF on the graphene template.

The surface charge property for RGO, COF, and COF/RGO composites was evaluated using zeta potential measurements. As shown in Figure S17, all the samples have negative zeta potential values. The zeta potential of RGO is −26.9 mV, arising from the small amount of oxygen-containing groups on the surface (O/C atom ratio = 0.19 from XPS analysis, Figure S6). The COF sample, on the other hand, has a more negative potential of −39.3 mV due to the large amount of electronegative $-SO_3^-$ groups on its backbone. For CGA samples, with increasing COF loading, stronger electronegativities are observed; −34.9, −36.7, −38.0, and −38.1 mV for CGA-3.3, CGA-3.8, CGA-4.6, and CGA-5.5, respectively (Figure S17). Therefore, these materials are potential candidates for the adsorption of positively charged organic pollutants through electrostatic interactions. On the basis of the surface charge and pore size of COF-SO_3Na, three kinds of common cationic dyes with different sizes were selected to evaluate the accessibility of dyes to the adsorbents. The dyes include, compared to the pore size of COF-SO_3Na (13.6 Å), a larger molecule (Rhodamine B, RhB, 16.6 Å × 13.5 Å), a smaller molecule (Methylene Blue, MB, 15.8 Å × 8.5 Å) and a similar-sized molecule (Crystal Violet, CV, 13.6 Å × 13.7 Å) (Figure 3a).

The adsorption isotherms and adsorption kinetics for dye pollutants were investigated by introducing 5 mg of a given material into a 5 mL aliquot of each aqueous dye

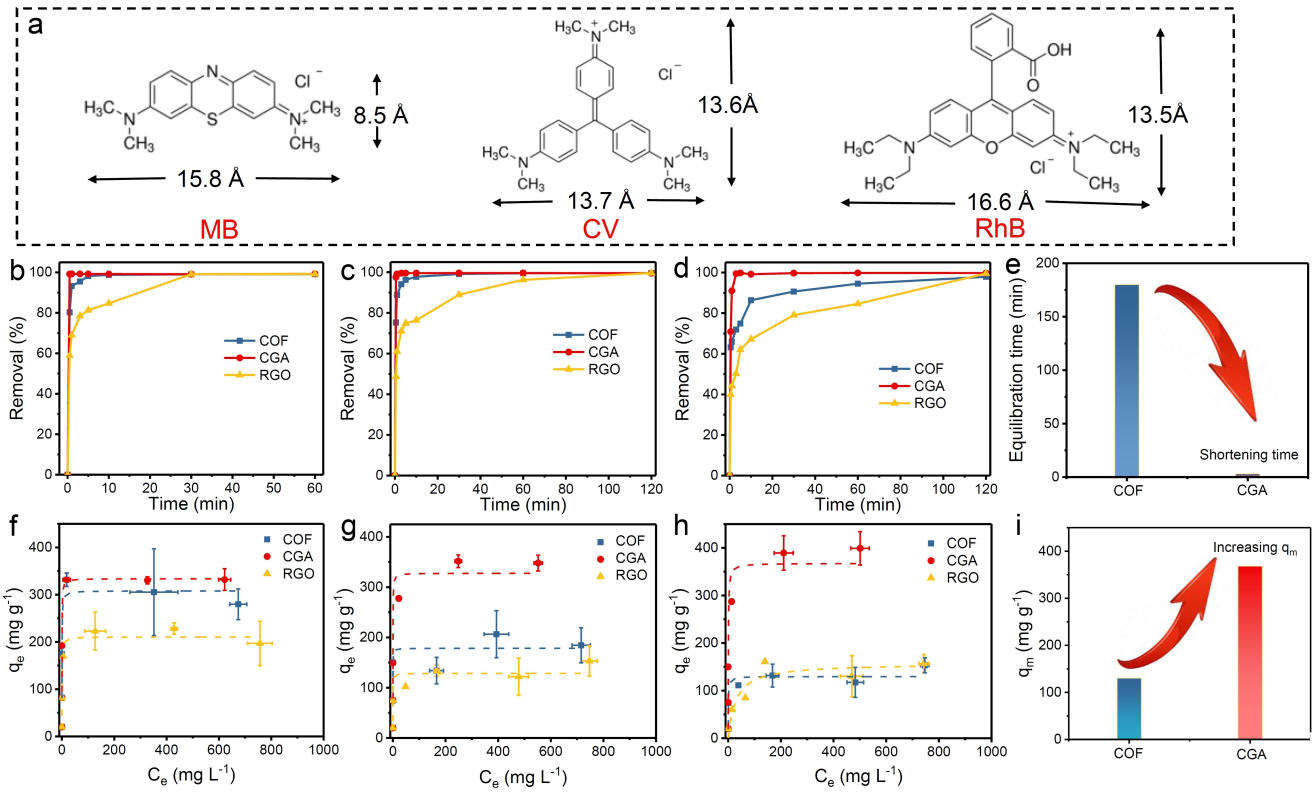

Figure 3. a) Chemical structures of organic dyes used in this study. Adsorption kinetics of CGA for b) MB, c) CV, and d) RhB. e) Comparison of equilibrium times of COF powder and CGA for RhB adsorption. Adsorption isotherms of CGA at room temperature for f) MB, g) CV, and h) RhB. i) Comparison of the maximum RhB adsorption capacities of the COF powder and CGA.

solution at room temperature for a certain time, followed by separating the sorbents through filtration (see Supporting Information for more experimental details). UV/Vis spectroscopy was then used to analyze the concentration of the filtrate. The effect of COF layer thickness on the adsorption performance was studied preliminarily (Figures S18–S21). Unsurprisingly, the equilibrium uptake capacity increases with the amount of COF due to the increasing electrostatic attraction. Nevertheless, CGA-5.5 shows a small decrease in capacity likely because the increasing layers led to insufficient binding site availability. Thus, CGA with a thickness of 4.6 nm achieves the highest capture performance for the three dyes (Figure S18 and Table S4). To elucidate the key role that the ultrathin COF plays in the adsorption process, COF powder and RGO were also employed as sorbents in control experiments. The adsorption kinetics were studied with an initial dye concentration of 20 $mg\,L^{-1}$ at different time intervals (Figure 3b–d). Among the three materials, CGA and COF present much faster sorption kinetics than RGO possibly due to their stronger electrostatic interactions with the three cationic dyes. CGA demonstrates the highest removal efficiency, which can reach above 90 % within 1 min irrespective of the dye molecular size (MB 99 %, CV 99 %, and RhB 91 %). In contrast, the COF powder could only remove 93 % of MB, 89 % of CV and 66 % of RhB, respectively, from water within the same time. Moreover, the time to reach equilibrium for COF increases with the dye molecular size, i.e., 3 min, 30 min, and 180 min for MB, CV, and RhB, respectively (Figures 3b–d and S22). This phenomenon reveals that ultrathin COF can tremendously shorten the time required to reach equilibrium, especially for larger pollutant molecules (Figure 3e).

Adsorption isotherms were constructed by introducing the adsorbents into the dye solution with varied initial dye concentrations (20–900 $mg\,L^{-1}$). The resulting data were fit to a Langmuir model to determine the maximum capacity, and the detailed fitting parameters are shown in Table S4. Overall, all three materials do adsorb the three cationic dyes. RGO displays the lowest adsorption capacity due to its less negative charge. The COF powder shows that the dye adsorption decreases with increasing dye size (308 $mg\,g^{-1}$ for MB, 178 $mg\,g^{-1}$ for CV, and 130 $mg\,g^{-1}$ for RhB). Remarkably, CGA demonstrates the highest uptake capacity for all the three pollutants (334 $mg\,g^{-1}$ for MB, 328 $mg\,g^{-1}$ for CV, and 368 $mg\,g^{-1}$ for RhB, respectively). These results demonstrate that CGA has the ability to adsorb organic dyes from water regardless of their size. In addition, it should be noted that with the increase in the size of dye molecules, the enhancement of adsorption capacity compared to pure COF becomes more prominent. Especially for the largest RhB molecule, the maximum capacity of CGA is close to three times higher than that of COF powder (Figure 3i). The maximum uptake of RhB by CGA is even higher than that of the previously reported 3D-printed COF-GO foams (194 $mg\,g^{-1}$),[34] MOF aerogel (81 $mg\,g^{-1}$),[8] and commercially available activated carbon (58–87 $mg\,g^{-1}$).[35] To illustrate the potential real-world utility of CGA, RhB was employed as a model dye to investigate the pH effect and sorbent recyclability (Figure S23). The removal efficiency across a range of pH conditions remains above 99 %. Meanwhile, the CGA can maintain the original removal efficiency for at least 5 adsorption/desorption cycles. CGA could therefore be a good candidate as a water remediation material.

To elucidate the adsorption mechanism, the interaction between COF and RhB on the graphene surface (Figure S24) has been modeled using density functional theory (DFT) by considering two representative orientations between COF and RhB (Conformation-1 and Conformation-2, Figure S25). In Conformation-1 (Figure S26), COF can interact with RhB through the H atom attached to the N atom of the COF backbone with the Cl^- of RhB to form the N–H···Cl hydrogen bond (H-bonding, the H-bond energy is $-6.690\,kcal\,mol^{-1}$), and through the O atom of $-SO_3$ attached to the benzene ring of COF with the H atom of –COOH in RhB to form the S–O···H H-bond (the H-bond energy is $-12.014\,kcal\,mol^{-1}$). In Conformation-2 (Figure S27), COF interacts with RhB through the O atom attached to the benzene ring of COF and the H atom of –COOH in RhB to form the C–O···H H-bond (the H-bond energy is $-10.109\,kcal\,mol^{-1}$), and through the N–H···Cl H-bond ($-6.391\,kcal\,mol^{-1}$) similar to that in Conformation-1. Apart from the intermolecular H-bonds (the blue of the color-filled reduced density gradient (RDG) isosurface map in Figure S28), one also observes a weaker C_π–H···Cl H-bond in RhB itself (near -2.000 to $-3.000\,kcal\,mol^{-1}$). Moreover, the intermolecular weak interaction analysis using the noncovalent interaction method (NCI, as detailed in Supporting Information) indicates that there are π–π stacking interactions between COF/graphene and RhB (the green of the RDG isosurface map in Figure S28), suggesting a stable sorption at the interface. In total, the binding energy (E_b) of COF and RhB is $-56.013\,kcal\,mol^{-1}$ in Conformation-1, and $-63.999\,kcal\,mol^{-1}$ in Conformation-2. Consequently, in addition to electrostatic interactions, intermolecular H-bonds and π–π stacking interactions also contribute to RhB sorption by the novel COF/graphene composite.

Further investigations into the adsorption mechanism were carried out using anionic dyes [Congo Red (CR) and Methyl Orange (MO), Figure S29] and COFs without charged groups (TpPa-COF, Pa = *p*-phenylenediamine and TpBD-COF, BD = benzidine, Figures S30 and S31). Complete experimental details are available in the Supporting Information. As shown in Figure S29, the cationic dyes (RhB, MB and CV) appear to be more efficiently captured by CGA. Despite electrostatic repulsions, CGA still displayed an adsorption for anionic dyes (CR and MO), which can be attributed to H-bonding and π–π interactions. CR has a more conjugated structure which led to a higher uptake capacity than for MO. To illustrate the effect of the surface charge of COFs, TpPa-COF and TpBD-COF (Figure S30a, d) were prepared in order to study their adsorption capacity. The XRD patterns confirm the formation of the crystalline structure of TpPa-COF and TpBD-COF (Figure S30b, e). N_2 sorption measurements were performed to determine the specific surface area (Figure S30c, f). TpPa-COF and TpBD-COF exhibit large S_{BET} values, which are 805 and 686 $m^2\,g^{-1}$, respectively. Despite the larger surface area, TpPa-COF

with similar pore size to COF-SO_3Na still shows much lower uptake capacity. TpBD-COF with large pore size displays a slightly lower, but very close adsorption capacity to COF-SO_3Na. The adsorption of RhB on TpPa-COF and TpBD-COF can be attributed to H-bonding and π–π interactions. These experiments demonstrate that H-bonding and π–π interactions could also be responsible for the observed adsorption, which agrees well with the theoretical calculations.

The improvement in performance of the CGA compared to the COF powder can be explained as follows. Firstly, due to the 3D continuous macroporous channels within ultralow density hybrid aerogel, pollutants are able to diffuse rapidly into the channels, which increases access to the micropores in the COF structure. Thus, CGA exhibits rapid removal of various dyes. However, in the case of the COF powder, their highly stacked 2D structures and lack of macropores mean that their inner surfaces are less accessible for target molecular species, and therefore they require long time periods to reach their adsorption capacity. Secondly, the COF powder only allows dyes (e.g., MB) with a molecular size much smaller than the pore size (1.36 nm) to enter the COF channels, while the larger dyes (e.g., CV or RhB) have difficulty reaching the interior adsorption sites. In other words, COF can only adsorb the larger dyes on its crystallite surface. Ultrathin COF, on the other hand, provides maximum adsorption site exposure, which enables more efficient adsorption of larger target molecules than the bulk counterpart, resulting in high uptake capacities for various dyes. The mechanism of this difference is illustrated in Scheme 1. Finally, in the composite aerogel, COF and RGO synergistically furnish negative charge and conjugate structure on the material surface, which are beneficial for the association of guest molecules with the adsorbent through electrostatic attraction, intermolecular H-bonding and π–π interactions. Therefore, the interlinked macroporous architecture decorated with ultrathin COF micropores makes the hybrid aerogel a suitable candidate for enhanced, ultrafast pollutant capture.

Conclusion

In conclusion, an ultrathin anionic COF has been constructed homogeneously on the surface of a graphene template. The interconnected graphene nanosheets not only offer 3D macroporous channels, but also serve as a 2D template to support the uniform growth of the COF to a thickness of ca. 2 nm. The synergy between the 3D graphene and 2D ultrathin COF can accelerate mass transport and improve the adsorption capacity for dyes irrespective of their size. Moreover, for the first time, the relationship between COF layer thickness and adsorption performance was investigated. Compared to bulk COF powder, the anionic ultrathin COF exhibits shortened time to equilibrium and increased adsorption capacity for the removal of cationic organic dyes of different sizes owing to the maximum exposure of active sites. This work demonstrates a green, facile, and effective approach for the fabrication of ultrathin COFs, which can act as an ideal model to further explore the structure–performance relationship of these materials at atomic levels and provide useful insights for their applications, even beyond the adsorption of organics.

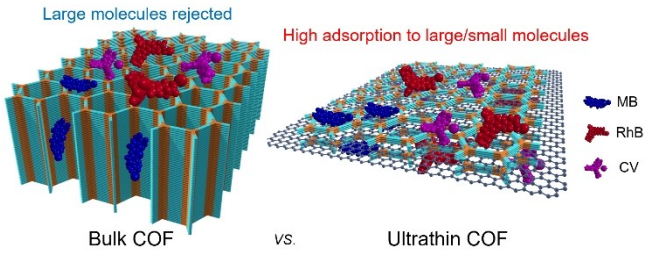

Scheme 1. Illustration of the dye adsorption mechanism on bulk COF and ultrathin COF.

Acknowledgements

The authors thank the funding support of the University of Vienna, Austria. The authors thank Mag. Johannes Theiner (Faculty of Chemistry, University of Vienna) for performing elemental analysis. The authors acknowledge the help from Dr. Aaron Brewer (Department of Inorganic Chemistry—Functional Materials, University of Vienna) for the proofreading of the manuscript.

Conflict of Interest

The authors declare no conflict of interest.

Data Availability Statement

The data that support the findings of this study are available from the corresponding author upon reasonable request.

Keywords: Aerogel · Covalent Organic Frameworks · Graphene · Organic Pollutants · Ultrathin Materials

[1] P. J. J. Alvarez, C. K. Chan, M. Elimelech, N. J. Halas, D. Villagran, *Nat. Nanotechnol.* **2018**, *13*, 634–641.
[2] Y. Zhou, J. Lu, Y. Zhou, Y. Liu, *Environ. Pollut.* **2019**, *252*, 352–365.
[3] X. Liu, H. Pang, X. Liu, Q. Li, N. Zhang, L. Mao, M. Qiu, B. Hu, H. Yang, X. Wang, *Innovation* **2021**, *2*, 100076.
[4] P. L. Yap, K. Hassan, Y. L. Auyoong, N. Mansouri, F. Farivar, D. N. H. Tran, D. Losic, *Adv. Mater. Interfaces* **2020**, *7*, 2000664.
[5] R. Yu, Y. Shi, D. Yang, Y. Liu, J. Qu, Z.-Z. Yu, *ACS Appl. Mater. Interfaces* **2017**, *9*, 21809–21819.
[6] E. Alver, A. Ü. Metin, *Chem. Eng. J.* **2012**, *200*, 59–67.
[7] Y. Zhao, L. Wang, N. Fan, M. Han, G. Yang, L. Ma, *Cryst. Growth Des.* **2018**, *18*, 7114–7121.

[8] L. Zhu, L. Zong, X. Wu, M. Li, H. Wang, J. You, C. Li, *ACS Nano* **2018**, *12*, 4462–4468.
[9] Z.-W. Liu, C.-X. Cao, B.-H. Han, *J. Hazard. Mater.* **2019**, *367*, 348–355.
[10] Y. Li, C.-X. Yang, H.-L. Qian, X. Zhao, X.-P. Yan, *ACS Appl. Nano Mater.* **2019**, *2*, 7290–7298.
[11] B. Garai, D. Shetty, T. Skorjanc, F. Gándara, N. Naleem, S. Varghese, S. K. Sharma, M. Baias, R. Jagannathan, M. A. Olson, S. Kirmizialtin, A. Trabolsi, *J. Am. Chem. Soc.* **2021**, *143*, 3407–3415.
[12] S. Karak, K. Dey, A. Torris, A. Halder, S. Bera, F. Kanheerampockil, R. Banerjee, *J. Am. Chem. Soc.* **2019**, *141*, 7572–7581.
[13] D. Zhu, Y. Zhu, Q. Yan, M. Barnes, F. Liu, P. Yu, C.-P. Tseng, N. Tjahjono, P.-C. Huang, M. M. Rahman, E. Egap, P. M. Ajayan, R. Verduzco, *Chem. Mater.* **2021**, *33*, 4216–4224.
[14] Y. Li, W. Chen, W. Hao, Y. Li, L. Chen, *ACS Appl. Nano Mater.* **2018**, *1*, 4756–4761.
[15] X. Zhu, S. An, Y. Liu, J. Hu, H. Liu, C. Tian, S. Dai, X. Yang, H. Wang, C. W. Abney, S. Dai, *AIChE J.* **2017**, *63*, 3470–3478.
[16] N. Huang, P. Wang, D. L. Jiang, *Nat. Rev. Mater.* **2016**, *1*, 16068.
[17] C. S. Diercks, O. M. Yaghi, *Science* **2017**, *355*, eaal1585.
[18] A. Acharjya, P. Pachfule, J. Roeser, F.-J. Schmitt, A. Thomas, *Angew. Chem. Int. Ed.* **2019**, *58*, 14865–14870; *Angew. Chem.* **2019**, *131*, 15007–15012.
[19] P. Pachfule, A. Acharjya, J. Roeser, T. Langenhahn, M. Schwarze, R. Schomäcker, A. Thomas, J. Schmidt, *J. Am. Chem. Soc.* **2018**, *140*, 1423–1427.
[20] S. Kandambeth, B. P. Biswal, H. D. Chaudhari, K. Charan R-out, S. Kunjattu, H. S. Mitra, S. Karak, A. Das, R. Mukherjee, U. K. Kharul, R. Banerjee, *Adv. Mater.* **2017**, *29*, 1603945.
[21] D. Rodríguez-San-Miguel, C. Montoro, F. Zamora, *Chem. Soc. Rev.* **2020**, *49*, 2291–2302.
[22] J. Li, X. Jing, Q. Li, S. Li, X. Gao, X. Feng, B. Wang, *Chem. Soc. Rev.* **2020**, *49*, 3565.
[23] S. Wang, Q. Wang, P. Shao, Y. Han, X. Gao, L. Ma, S. Yuan, X. Ma, J. Zhou, X. Feng, B. Wang, *J. Am. Chem. Soc.* **2017**, *139*, 4258–4261.
[24] S. Gan, X. Tong, Y. Zhang, J. Wu, Y. Hu, A. Yuan, *Adv. Funct. Mater.* **2019**, *29*, 1902757.
[25] H. Chen, H. Tu, C. Hu, Y. Liu, D. Dong, Y. Sun, Y. Dai, S. Wang, H. Qian, Z. Lin, L. Chen, *J. Am. Chem. Soc.* **2018**, *140*, 896–899.
[26] W. Dai, F. Shao, J. Szczerbinski, R. McCaffrey, R. Zenobi, Y. Jin, A. D. Schlüter, W. Zhang, *Angew. Chem. Int. Ed.* **2016**, *55*, 213–217; *Angew. Chem.* **2016**, *128*, 221–225.
[27] D. Zhou, X. Tan, H. Wu, L. Tian, M. Li, *Angew. Chem. Int. Ed.* **2019**, *58*, 1376–1381; *Angew. Chem.* **2019**, *131*, 1390–1395.
[28] Z. Guo, H. Jiang, H. Wu, L. Zhang, S. Song, Y. Chen, C. Zheng, Y. Ren, R. Zhao, Y. Li, Y. Yin, M. D. Guiver, Z. Jiang, *Angew. Chem. Int. Ed.* **2021**, *60*, 27078–27085; *Angew. Chem.* **2021**, *133*, 27284–27291.
[29] C. Chen, T. Joshi, H. Li, A. D. Chavez, Z. Pedramrazi, P.-N. Liu, H. Li, W. R. Dichtel, J.-L. Bredas, M. F. Crommie, *ACS Nano* **2018**, *12*, 385–391.
[30] C. Li, J. Yang, P. Pachfule, S. Li, M.-Y. Ye, J. Schmidt, A. Thomas, *Nat. Commun.* **2020**, *11*, 4712.
[31] T. Chen, B. Li, W. Huang, C. Lin, G. Li, H. Ren, Y. Wu, S. Chen, W. Zhang, H. Ma, *Sep. Purif. Technol.* **2021**, *256*, 117787.
[32] Y. Peng, Z. Hu, Y. Gao, D. Yuan, Z. Kang, Y. Qian, N. Yan, D. Zhao, *ChemSusChem* **2015**, *8*, 3208–3212.
[33] S. Chandra, T. Kundu, K. Dey, M. Addicoat, T. Heine, R. Banerjee, *Chem. Mater.* **2016**, *28*, 1489–1494.
[34] A. K. Mohammed, S. Usgaonkar, F. Kanheerampockil, S. Karak, A. Halder, M. Tharkar, M. Addicoat, T. G. Ajithkumar, R. Banerjee, *J. Am. Chem. Soc.* **2020**, *142*, 8252–8261.
[35] K. Jedynak, D. Wideł, N. Rędzia, *Carbon Colloids Interfaces* **2019**, *3*, 30.

Manuscript received: May 4, 2022
Accepted manuscript online: May 31, 2022
Version of record online: July 4, 2022